



**HAL**  
open science

## Lab demonstration of wavefront reconstruction for the fragmented aperture of the ELT

Arielle Bertrou-Cantou, Eric Gendron, Gérard Rousset, Fabrice Vidal, Jordan Raffard, Arnaud Sevin, Florian Ferreira, Yann Clenet

► **To cite this version:**

Arielle Bertrou-Cantou, Eric Gendron, Gérard Rousset, Fabrice Vidal, Jordan Raffard, et al.. Lab demonstration of wavefront reconstruction for the fragmented aperture of the ELT. Adaptive Optics for Extremely Large Telescopes 7th Edition, ONERA, Jun 2023, Avignon, France. 10.13009/AO4ELT7-2023-126 . hal-04402863

**HAL Id: hal-04402863**

**<https://hal.science/hal-04402863>**

Submitted on 18 Jan 2024

**HAL** is a multi-disciplinary open access archive for the deposit and dissemination of scientific research documents, whether they are published or not. The documents may come from teaching and research institutions in France or abroad, or from public or private research centers.

L'archive ouverte pluridisciplinaire **HAL**, est destinée au dépôt et à la diffusion de documents scientifiques de niveau recherche, publiés ou non, émanant des établissements d'enseignement et de recherche français ou étrangers, des laboratoires publics ou privés.



## Lab demonstration of wavefront reconstruction for the fragmented aperture of the ELT

Arielle Bertrou-Cantou<sup>a, b</sup>, Eric Gendron<sup>b</sup>, Gérard Rousset<sup>b</sup>, Fabrice Vidal<sup>b</sup>, Jordan Raffard<sup>b</sup>, Arnaud Sevin<sup>b</sup>, Florian Ferreira<sup>b</sup>, and Yann Clénet<sup>b</sup>

<sup>a</sup>Department of Astronomy, California Institute of Technology, 1200 E. California Blvd., Pasadena, CA 91125, USA

<sup>b</sup>LESIA, Observatoire de Paris, Université PSL, CNRS, Sorbonne Université, Université de Paris, 5 place Jules Janssen, 92195 Meudon, France

### ABSTRACT

The fragmentation of the ELT pupil in six petals (or fragments) by the spider presents a unique challenge in implementing adaptive optics (AO) systems for the instruments: the spider arms break the spatial continuity of the incoming wavefront. In visible light, the pyramid wavefront sensor (WFS) was shown to be a poor candidate to reconstruct the differential pistons between each fragments. Assuming spatial continuity of the incoming wavefront or applying Kolmogorov statistical theory of turbulence (no Low Wind Effect), a well-chosen control strategy can successfully reconstruct the entire wavefront. The SESAME testbed at LESIA enables to reproduce the relevant characteristics of the ELT (pupil fragmentation, high order DM). By replicating seeing conditions typical of Cerro Armazones, we demonstrate in-lab control strategies that effectively reconstruct the full continuous wavefront. Performance comparisons are made with a regular AO loop relying solely on the Pyramid WFS measurements.

**Keywords:** Wavefront sensing and control, fragmented pupil, pyramid wavefront sensor.

### 1. INTRODUCTION

The pyramid wavefront sensor (P-WFS) is the favorite choice for all adaptive optics (AO) systems that will equip the first light instruments of the Extremely Large Telescope (ELT) [7] [13] [4]. However, it was demonstrated that it is poorly sensitive to differential pistons, a type of aberrations that becomes critical when considering the strong fragmentation of the ELT telescope pupil by its spider. Not only the differential piston signal undergoes a loss in sensitivity, but a modal confusion also impairs the wavefront (WF) reconstruction [1]. In the most severe atmospheric condition, the sensitivity loss is so large that a reconstruction based on the P-WFS measurements becomes vain. Based on this observation, several strategies have been considered in order to circumvent these difficulties and to provide a continuous reconstruction of the WF. We can cite the pairing method [14] as well as the MAP reconstructor [12]. Similarly, in [1] and [3], two other methods were proposed: one that restraint the divergence of the poorly sensed actuators, and another based on a MMSE reconstructor. This proceeding aims at reporting the in-lab results of a closed-loop AO system, using the two latter reconstruction methods and to compare them with a regular loop that only relies on the P-WFS measurements, with conditions that closely

match the ones encountered on the ELT. The experimental work was conducted on the SESAME testbed, which provides all the necessary tools to implement and develop novel AO WF sensing and control strategies.

The first part of this proceeding (Section 2) covers the description of the testbed and the demonstration of a closed loop using the high order ALPAO deformable mirror (DM). The second part (Section 3 to 5) is dedicated to the implementation of the relevant characteristics of the ELT (including its fragmented pupil) and of the AO control strategies, to finally ends up on the closed-loop experimental results.

This proceeding presents experimental results that were previously published in the context of this PhD thesis [2] and freely reuses most of the content presented in this dissertation.

## 2. THE SESAME TESTBED: A HIGH ORDER AO DEMONSTRATOR

### 2.1 Testbed Description

The SESAME bench serves as a host platform to develop AO systems for future ground-based telescopes. Its primary objective is to facilitate the integration of new concepts in AO and wavefront correction methods, such as tomography [15]. To support the technology development of AO in the context of the Extremely Large Telescopes (ELTs), the PYRCADO (PYRramid for miCADO) experiment was initiated on the SESAME bench in the years 2014 and 2015 [6]. Equipped with a P-WFS and, since 2019, a high-order DM with 3228 actuators by ALPAO [16], this experiment contributes to the development of Single-Conjugate Adaptive Optics (SCAO) for the MICADO instrument. In 2020, the real-time computer (RTC) from the COSMIC platform was integrated into the SESAME bench [9].

The optical layout is presented in Figure 1. The source assembly consists of a HeNe laser ( $\lambda = 633 \text{ nm}$ ) with a  $20 \mu\text{m}$  pinhole as a spatial filter to improve the quality of the beam, yielding a quasi-Gaussian beam profile.

Three optical components are placed in collimated beam and act on the phase of the light: a high order DM with 3228 actuators (64 across the pupil), a spatial light modulator (SLM) and a mirror held in a gimbal mount to compensate for large tip/tilt wavefront errors. The SLM is placed after a linear polarizer as it is a polarization-sensitive device. Unlike the two other mirrors, its action is strictly monochromatic. Comprising a large number of pixels, with a screen of  $800 \times 600$ , its resolution enables correction across a wide range of spatial frequencies. The effective correction zone defined by the pupil illumination is of size 504 pixels.

SESAME owns several sensors including a Shack-Hartmann WFS and a reflective pyramidal WFS [5]. The sensor of interest here is the PYRCADO WFS consisting of: a fast steering mirror which modulates the incoming beam, a pyramidal prism placed in the focal plane and a pupil imaging lens (PIL). A CMOS detector Manta G-235 from Allied Vision enables imaging of the 4 pupils of the PWFS. This same detector is also used after one of the beamsplitters in the optical path to acquire the "scientific" PSF images shown later.

### 2.2 Semi-synthetic model for interaction matrices

Although they should possess the same properties in theory, the influence functions of the ALPAO DM actuators do not exhibit an identical response across the entire pupil. This discrepancy arises either because their proximity to the pupil's edge makes them weakly visible or due to their recalcitrant nature (fabrication). The presence of these singular actuators biases the inversion of the interaction matrix (IM)  $\mathbf{D}$  and prevents the computation of a "clean" reconstructor. The semi-synthetic zonal IM model, as detailed subsequently, is based on a proposition by E. Gendron [10]. It enforces the resemblance of the response from each actuator and thus assumes isotropic influence functions across the pupil. The model needs an experimental zonal IM  $\mathbf{D}_z$  as starting point, the semi-synthetic response is built following these four steps:

1. Identification of the position of the DM actuators in the sensor pupil plane: from the zonal matrix  $\mathbf{D}_z$ , an actuator is chosen to be the reference (here, the actuator with index 1640), and the relative position of the other actuators with respect to this reference is deduced by correlation, with a sub-pixel accuracy.
2. Finer adjustment of the actuator positions assuming a square grid of the DM, accounting for possible homotheties, translations, and rotations relative to the theoretical actuator grid.

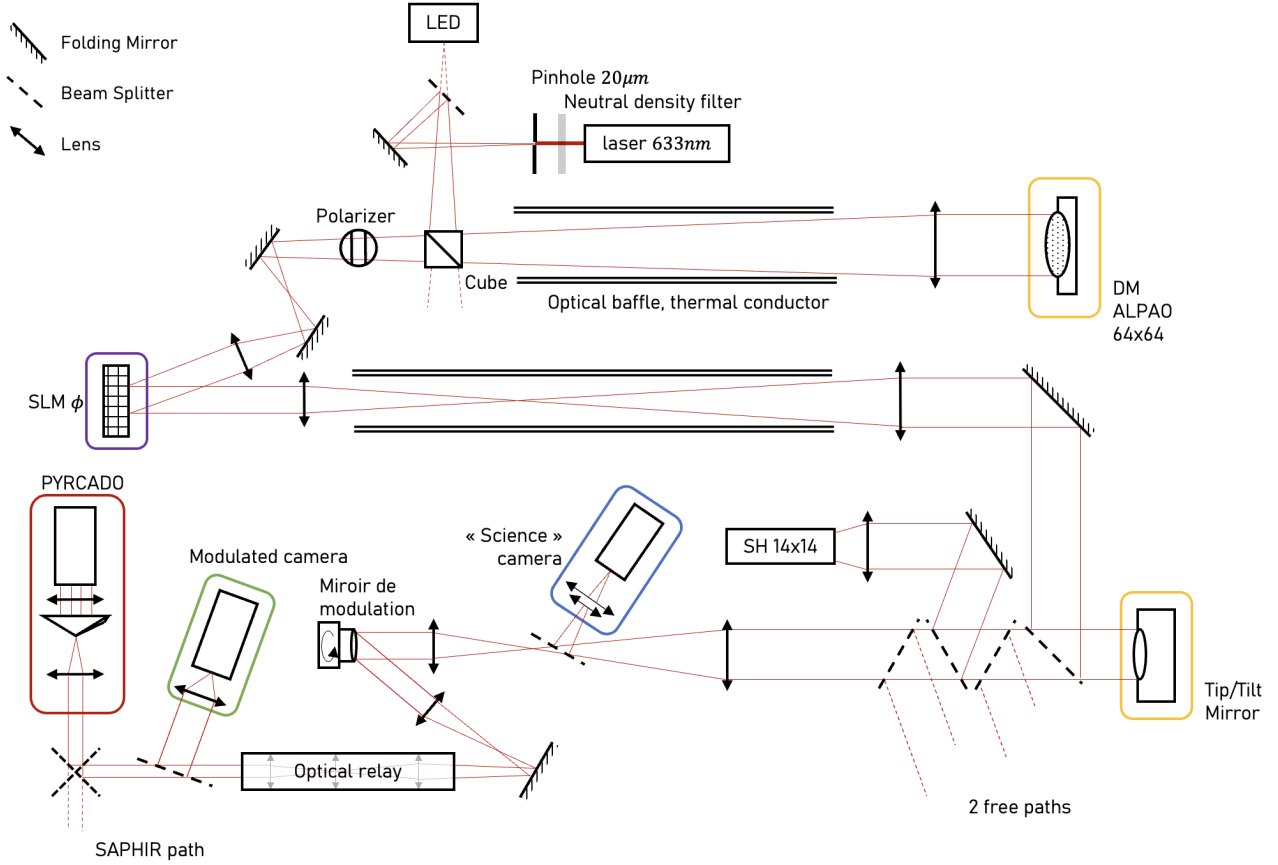


Figure 1. Optical path and components of the SESAME testbed.

3. Selection of the best actuators from the panel, here using 75% of the actuators whose response in  $D_z$  is similar to that of the reference actuator. A synthetic response is computed by averaging their responses. This operation is carried out while ensuring a proper alignment of each actuator responses to a same center, by translation of the actuator response functions and using a Fourier transform.
4. The final step involves copying the calibrated synthetic response from step 3 to all the actuators, knowing their precise center positions in the sensor plane from step 2. This is done using translations of the synthetic response across the entire pupil.

The semi-synthetic zonal IM for all DM actuators is noted as  $D_{zsn}$ . Any modal reconstructor can then be derived for a given modal basis  $B$  using the formula:  $(D_{zsn}B^t)^\dagger$ . We note that this proposition is an extension of the pseudo-synthetic approach proposed in [11], aiming at coping with the DM mis-registrations and at generating noise-free IM.

For the scope of this work, the modal basis is based on a simplified Karhunen–Loève (KL) basis [1]. TT modes are projected on the TT DM while the other modes are controlled by the ALPAO DM.

### 2.3 Closed loop results with the ALPAO kilo-DM

To close the loop with the ALPAO DM, we used the P-WFS with a modulation of  $3 \lambda/D$ . Figure 2 shows qualitative preliminary results, obtained in late 2020, when closing the loop on the 2000 first modes of the ALPAO DM and using a prototype of the COSMIC RTC (ref). The atmospheric turbulence is here characterized with a Fried parameter  $r_0 = 20 \text{ cm}$  given at  $500 \text{ nm}$  assuming a telescope pupil of  $20 \text{ m}$ . In other words, for the ALPAO

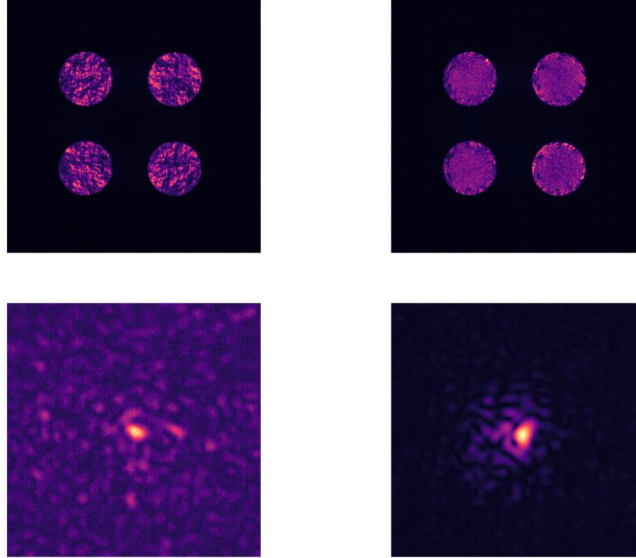


Figure 2. P-WFS and PSF images of **Left** open-loop and **Right** closed-loop AO system controlling 2000 modes of the ALPAO DM with a turbulence characterized by  $d_{act}/r_0 = 1.2$ . The bright spot on the open-loop PSF image corresponds to a ghost reflection of the SLM.

DM, the  $d_{act}/r_0$  ratio is of 1.2. On the open-loop image, we can clearly see a ghost reflection that is due to the SLM, the atmospheric speckles are distributed over the whole field of view. The closed-loop image shows a main coherent core while some residual speckles, mainly low orders, are still present. We note that no optical gain compensation method was used. Further work has been later performed in order to improve the quality of the reconstruction, with more controlled modes, hence lower AO residuals, and for seeing conditions closer to Cerro Armazones, with  $d_{act}/r_0 \approx 2$ .

### 3. IMPLEMENTATION OF THE ELT GEOMETRY

The ALPAO DM and its 3228 actuators exhibits a similar actuator density to the M4 DM of the Extremely Large Telescope (ELT). However, it consists of a single piece of mirror and its influence functions are not representative of the ones of M4. Hence, this mirror was not suitable to measure and characterize the petal modes while considering a fragmented geometry similar to the ELT. This section explains how the SLM was used for its primary role first, i.e. to generate atmospheric phase screens, but also for introducing a fragmented geometry at the telescope pupil level and at the DM level. The constraint imposed by the number of usable pixels on the SLM led to a revision of the ELT's DM geometry. To accommodate this limitation, the decision was made to reduce the pupil's diameter by half while keeping the density, inter-actuator spacing, and influence functions of the DM unchanged.

#### 3.1 Atmospheric phase screens

Turbulent phase screens are generated using a layer of the COMPASS software, using the von Kármán model. An external scale is provided to the model, with  $L_0 = 25 \text{ m}$ , in addition to the Fried parameter  $r_0$ . Here, a single turbulent layer is generated, we assume it is closed to the ground and conjugated to the pupil, evolving at a velocity  $|v|$  according to the Taylor hypothesis (frozen flow assumption). The simulated telescope aperture is set to 20 m. Given the number of pixel elements of the SLM, the chosen configuration yields a resolution of 4 cm per pixel. To ensure proper sampling of the turbulent phase screen, a requirement of at least 3 pixels per  $r_0$  is set, given at the wavelength of the bench,  $\lambda_0$ . Hence, the setup allows for the simulation of  $r_0$  values up to 12 cm at  $\lambda_0$ , corresponding to  $r_0 = 9 \text{ cm}$  at 500 nm.

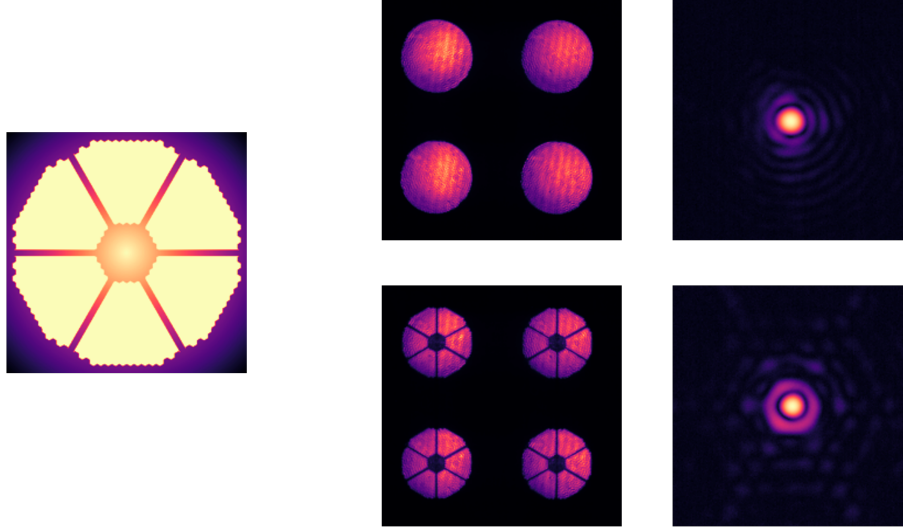


Figure 3. **Left** Phase applied on the SLM to mimic the amplitude variations of the ELT, and **Right** P-WFS plane and PSF images before and after implementation of the ELT pupil geometry.

### 3.2 Fragmented and obscured pupil

The SLM is capable of modulation of the phase exclusively. To achieve the required amplitude variations to simulate a telescope pupil mask, we chose to apply a significant tilt across the entire area where a null amplitude is desired. This effectively reflects the light outside of the pupil. To ensure optimal light rejection, a radial tilt is used from the center of the pupil, with steps of  $\lambda/4$  between each pixel of the SLM. This approach is particularly suited for a circular pupil geometry and when reproducing relatively thin spider arms. Figure 3 presents the phase mask applied to the SLM, along with the PYRCADO and the "scientific" detector images. The sensor images were obtained using a largely modulated beam to emphasize the obstruction by the secondary mirror and the spider arms (doing so minimizes diffractive behavior of the P-WFS). Distinct diffraction spikes and a hexagonal shape can be seen on the PSF image, respectively explained by the presence of the spider arms and the ELT pupil outer geometry. On the other hand, the brighter secondary lobe of the PSF is caused by the central obstruction of the pupil.

### 3.3 Deformable mirror

For a half telescope pupil size, the DM influence functions provided by ESO, accounting for 72 actuators across the pupil, couldn't be used. Hence, we derive them from an analytical model, based on Gaussian shape influence function. This model is provided in Appendix A of [2]. The result is a fragmented DM made of six petals, each featuring a triangular actuator grid with an inter-actuator spacing of  $0.54 m$  and no inter-actuator coupling of the influence functions. The DM has 1218 actuators, their coordinates projected on the entrance pupil space are illustrated in Figure 5. An outer ring of actuators lies beyond the effective, illuminated pupil of the telescope. These extra actuators ensure an accurate replication of the flat petal modes.

The final phase applied on the SLM is the addition of all these three contributions. A phase offset is applied to the phase map in order to minimize the number of  $2\pi$  jumps, related to the phase wrapping of the SLM.

We assume that the WF of the overall optical path of the SESAME testbed can solely be explained by the phase applied on the SLM. This is obviously not strictly correct as turbulence from the lab room itself as well as thermo-mechanical deformations of the optics also affect the WF. The first few orders of the common path aberrations are compensated using the ALPAO DM. Nonetheless, we verified that the phase applied on the SLM closely corresponds to the actual phase error observed on the optical bench.

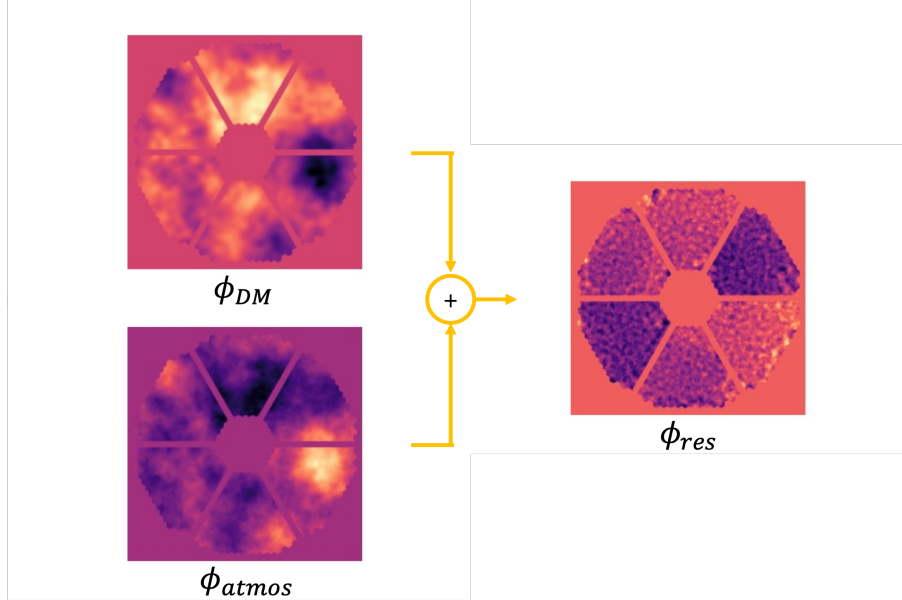


Figure 4. Example of atmospheric phase screen  $\phi_{atmos}$  and fragmented DM WF compensation  $\phi_{DM}$  that are summed and applied on the SLM as a single residual phase screen  $\phi_{res}$ . We note that this phase screen presents some differential pistons between each petal.

## 4. AO SYSTEM SET-UP AND CALIBRATION

### 4.1 Description of the modal basis

We aim at demonstrating and comparing the use of different control strategies in order to provide a WF reconstruction that deals with differential piston errors. A thorougher description of the methods can be found in the appropriate references, but the principle and objective of the three modal basis investigated in this work is briefly discussed here.

**Simplified KL Modes, or Gendron Modes  $B_r$**  The control of the petal modes relies solely on the measurement vector provided by the P-WFS. Orthogonal modes are computed for all actuators that appear in the illuminated pupil of the WFS, and are subsequently extended to the passive (out of pupil, yellow actuators on Figure 5) actuators, following the method described in [1].

**MMSE based reconstruction  $B_{mmse}$**  We use the same basis as  $B_r$  except that we filter out the petal modes, they are reconstructed using: the measurement vectors of all other orthogonal modes, and a prior knowledge of the statistics of the turbulence. This method was first introduced in [3] and then revised to provide better simulations results.

**Continuous basis  $B_c$**  The modal basis is computed in a same manner as the Simplified KL Modes, except that the actuators located along one side of the spider arms are now defined as passive actuators as well (in purple, Figure 5). There are a total of 84 passive actuators in this configuration, with 18 of them which overlap with the passive actuators of  $B_r$ . The modes are extended to the passive actuators using a Kolmogorov-type extensions [1]. By reducing the number of degrees of freedom, it prevents the injection of pure petal modes on the DM commands, hence reducing the divergence of these modes throughout the loop closure process. It's worth noting that the choice of the location and number of passive actuators can possibly be adjusted to improve wavefront reconstruction under varying seeing conditions.

The first two basis possess 864 degrees of freedom each, while the third one has 798 degrees of freedom. The modes of all three basis are expressed over the 1218 actuators of the DM, using a Kolmogorov-type extensions.

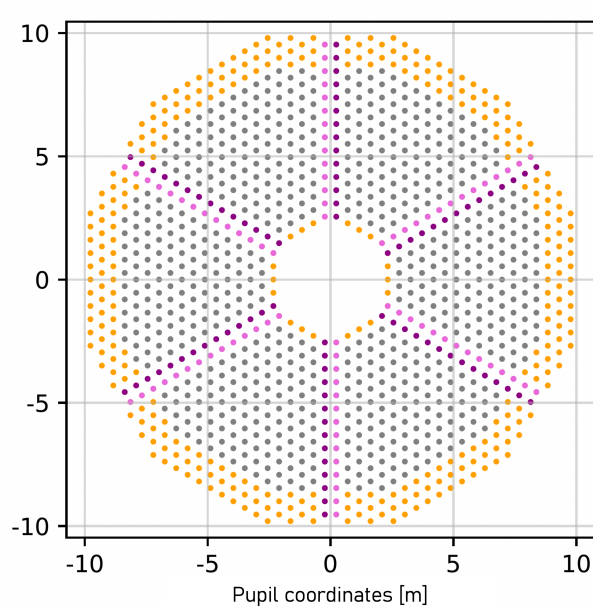


Figure 5. Actuator positions for a semi-ELT case with a pupil diameter of 20 m and an ELT-like inter-actuator pitch of  $d_{act} = 0.54$  m. There are a total of 1218 actuators, that is 203 per fragment. Gray actuators are within the illuminated pupil while yellow actuators are the prolongation of the DM at the very edge or outside of the effective pupil. Pink and purple actuators denote the actuators situated along the spider arms.

## 4.2 Adaptive Optics parameters

Table 1 summarizes the key parameters employed for this AO system. As previously detailed, the SLM is used to create an ELT-like telescope pupil with six arms of 54 cm, a central obstruction, and a 20 m diameter. Turbulence screens are generated with  $r_0$  values ranging from 12 cm to 30 cm to study various turbulence conditions, it covers both typical conditions observed at Cerro Armazones site (12 and 15 cm) and calmer conditions (20 and 30 cm).

The DM is a surrogate M4, replicating its main characteristics but cropped to a 20 m pupil diameter, featuring 36 actuators across the pupil diameter. The P-WFS operates with a HeNe laser point source and a  $3\lambda/D$  modulation radius. The pupil is sampled using 85 sub-apertures across the diameter, that is the sub-aperture to actuator ratio is 2.2, implying that the wavefront error is better sampled compared to the configuration envisioned for MICADO SCAO. Binning the pixels would however result in an insufficient sub-aperture to actuator ratio. We used a "full pixels" approach, not dealing with slopes computation and as envisaged in [8], to reduce errors related to misalignment: 22,704 measurement points per frame, corresponding to the pixels of all four pupils of the P-WFS camera, are sent to the RTC.

The controller is a regular integrator with a scalar gain of 0.6, this value was found to minimize the WF residuals for all atmospheric conditions. No optical gains compensation strategy was implemented here; that would be a possible point of improvement in the future. The theoretical loop frequency, that drives the atmospheric screen moving speed, is 500 Hz. However, the effective loop frequency on the bench, accounting for telemetry data acquisition at each iteration and communication times with the cameras, is of approximately 1 Hz. No extra latency is introduced in the loop: the DM voltages are applied at the frame following the measurement. The SLM's rise time, of the order of a few tens of milliseconds, is neglected here.

## 4.3 Interaction matrices and differential piston measurement

The method proposed earlier for the ALPAO DM to compute IM can't be applied here straightforwardly, as the ELT DM doesn't exhibit isotropic influence functions. For each basis introduced earlier, we derive an IM by averaging 10 IM measured on the testbed in order to smoothen the noise contribution. We use the "push-pull" method and the amplitude is adjusted so that each mode exhibits the same sensitivity: this means that we apply 40 nm RMS for tip/tilt commands whereas the commands of higher order modes are of the order of 10 nm RMS.

Telescope	ELT-like, $D = 20$ m 6 spider arms $t = 0.54$ m Central obstruction $0.28 D$
Turbulence	Single Layer von Kármán $r_0 = \{12, 15, 20, 30\}$ cm à 500 nm $L_0 = 25$ m $\ \mathbf{v}\  = 10$ m.s <sup>-1</sup>
DM (SLM)	$36 \times 36 = 1218$ actuators Hexagonal pattern, 6 floating shells Inter-actuator pitch $d_{act} = 54$ cm Null inter-actuator coupling Clip $\pm 8 \mu\text{m}$
P-WFS	$\lambda_{WFS} = 633$ nm Modulation $r_{mod} = 3 \frac{\lambda}{D}$ $85 \times 85$ subapertures = 22704 slopes
Controller	Integrator - $g = 0.6$ Loop frequency $f = 500$ Hz Null latency (Correction applied at frame + 1) Basis = $\{\mathbf{B}_r, \mathbf{B}_c, \mathbf{B}_{mmse}\}$

Table 1. Sizing of the semi-ELT geometry and parameters of the AO loop used on the SESAME testbed.

Doing so, we ensure that the IM is calibrated in the linear regime of the P-WFS and that the response to each mode has a sufficient signal to noise ratio. The IM have a condition number of  $1/20$ , we use a generalized inverse to compute the modal reconstructors. A same reconstructor  $\mathbf{D}_r^\dagger$  is used to control the basis  $\mathbf{B}_r$  and  $\mathbf{B}_{mmse}$  and matrix  $\mathbf{D}_c^\dagger$  is used for the basis  $\mathbf{B}_c$ .

## 5. EXPERIMENTAL RESULTS

The presented results are obtained in a closed-loop configuration, using residual phase applied on the SLM as knowledge of the current state of the AO loop.

The SLM suffers from a ghost image issue, which particularly affects the small  $r_0$  performance: as seen in Figure 2, a bright coherent core is seen among the speckles. Various methods were considered to shift this ghost, including the application a significant tilt to the SLM and the compensation for this tilt with a physical TT mirror. However, this approach would introduce numerous phase jumps due to the wrapped nature of the applied SLM tilt, and would significantly alters the reference vector of the P-WFS. Hence, we "live" with this ghost, acknowledging it is a strong limitation of our experimental results (it substantially adds to the challenges).

Figure 6 illustrates the evolution of differential pistons over 1000 iterations, equivalent to 2 seconds of atmospheric screen movement (16 minutes of bench acquisition). From left to right, the results for each petal mode compensation strategy,  $\mathbf{B}_r$ ,  $\mathbf{B}_{mmse}$ , and  $\mathbf{B}_c$ , are presented. Each row represents a different observing condition, with  $r_0$  expressed at 500 nm, ranging from 12, 15, 20, to 30 cm. We note that this was done for a sensor working at  $\lambda = 633$  nm so it typically operates at shorter wavelength than the AO systems of the ELT instruments. Dealing with  $r_0 = 20$  cm at  $\lambda = 633$  nm is like dealing with  $r_0 = 15$  cm at  $\lambda = 800$  nm.

When examining the results obtained with the  $\mathbf{B}_r$  basis, the most striking observation is the divergence of differential pistons at low  $r_0$  values. The control of these modes is unstable, unmeasured by the sensor. This observation is actually much more dramatic than what could be seen in simulations, where the behavior looked more like random fluctuations [1]. Moving towards larger  $r_0$  values, e.g.,  $r_0 = 20$  cm, we can notice that the differential pistons tend to stabilize around modulo  $\lambda$  values for several tens of iterations. With better seeing, i.e.,  $r_0 = 30$  cm, this stabilization extends over several hundred iterations.

The results which use petal mode control methods are clear: they effectively contribute to limit the divergence of these modes, and to get rid of the  $\lambda$  ambiguity problem. Whether using the "MMSE method" or the so-called "continuous" basis, the amplitude of differential piston fluctuations over time is much smaller than with a classical

AO control loop. However, we can still see how the performance decreases at the same time as the coherence degree of the phase on either side of the spiders, which itself decreases with  $r_0$ . For low  $r_0$  values, we note that while these methods prevent divergence in the control loop, the performance was still limited on our experiment by:

- the error in intra-petal correction; the observation vector could be further improved on the bench by using modal gains,
- it is possible that certain processes, like bench thermic fluctuations or control loop errors (single actuator divergence), introduce "non-Kolmogorov" errors that are poorly managed by the MMSE or the continuous basis.

To truly appreciate the value of petal modes control strategies, the best line to consider is the last one, corresponding to  $r_0 = 30 \text{ cm}$  and representing the best observing conditions. Here, all 5 curves fluctuate around 0, whereas the results with the basis  $\mathbf{B}_r$  basis show jumps of 1 to several wavelengths.

Figure 7 presents the residual phases of the SLM at the final iteration of the loop (iteration 1000). The scale is the same for each WF map at a given atmospheric condition. It clearly shows how the petal modes saturate when the P-WFS is used to control the petal modes. These maps allow qualitative observation, indicating that some actuators on the inner edge of the pupil tend to diverge. Without giving a complete explanation of the reason of poor petal mode correction at smaller  $r_0$ , we found at that these events significantly reduce the performance of control methods using  $\mathbf{B}_{mmse}$  and  $\mathbf{B}_c$ . A more strict definition of active actuators could be used in order to reduce this source of error.

## 6. CONCLUSIONS

Putting aside the issue of fragmentation, the work using the 3228-actuator ALPAO DM allowed for the validation of AO loop closures on a high-order system with the P-WFS (PYRCADO) and the COSMIC RTC prototype, which will be used for the MICADO instrument's SCAO. A semi-synthetic IM methods was proposed and was successfully implemented on the testbed in order to efficiently control a large number of modes.

Using the SLM present on the SESAME bench, we replicated key ELT parameters, including its pupil mask (obstruction and fragmentation) and its DM (actuator density, influence functions). We conducted experiments using atmospheric conditions that are representative of the ones encountered on Cerro Armazones. We highlighted the challenges faced by the P-WFS in providing reliable measurements of petal modes, which were exacerbated by real-life bench conditions. This manifests as - from best to worst case scenarios: phase jumps and random fluctuations of the differential pistons, to a complete divergence of the petal modes, leading to saturation of the DM commands.

We demonstrated two reconstruction methods based on the assumption of a continuous corrugated WF, and which specifically target the divergence of the petal modes: differential piston fluctuations were generally contained within  $\pm\lambda_{WFS}$  even for poor seeing conditions. While the continuous basis method was favored in experiments, we can't really distinguish it from the MMSE method. The effectiveness of these methods is confirmed at two levels: for the stability of the AO control loop on one hand, and in terms of image quality for the science channel on the other hand. These results are very encouraging, especially considering the limitations specific to our testbed, such as the SLM's ghost reflection, and the potential future improvements, including the implementation of optical gains.

Finally, we point out that these methods were implemented in order to deal with differential pistons that follow the Kolmogorov spectrum, they will not supplement an appropriate and accurate measurement of petal modes when dealing with non-Kolmogorov disturbances. These concerns stem from various sources, starting with the Low Wind Effect phenomenon, but not limited to it: opto-mechanical misalignments, co-phasing errors, etc. This issue could quickly becomes critical for all of ELT's first-light instruments and, if "continuous" method of WF reconstruction are considered, it is crucial to gain a deeper understanding on how non-Kolmogorov errors would interact with the P-WFS measurements and the reconstruction methods that are based on wavefront continuity.

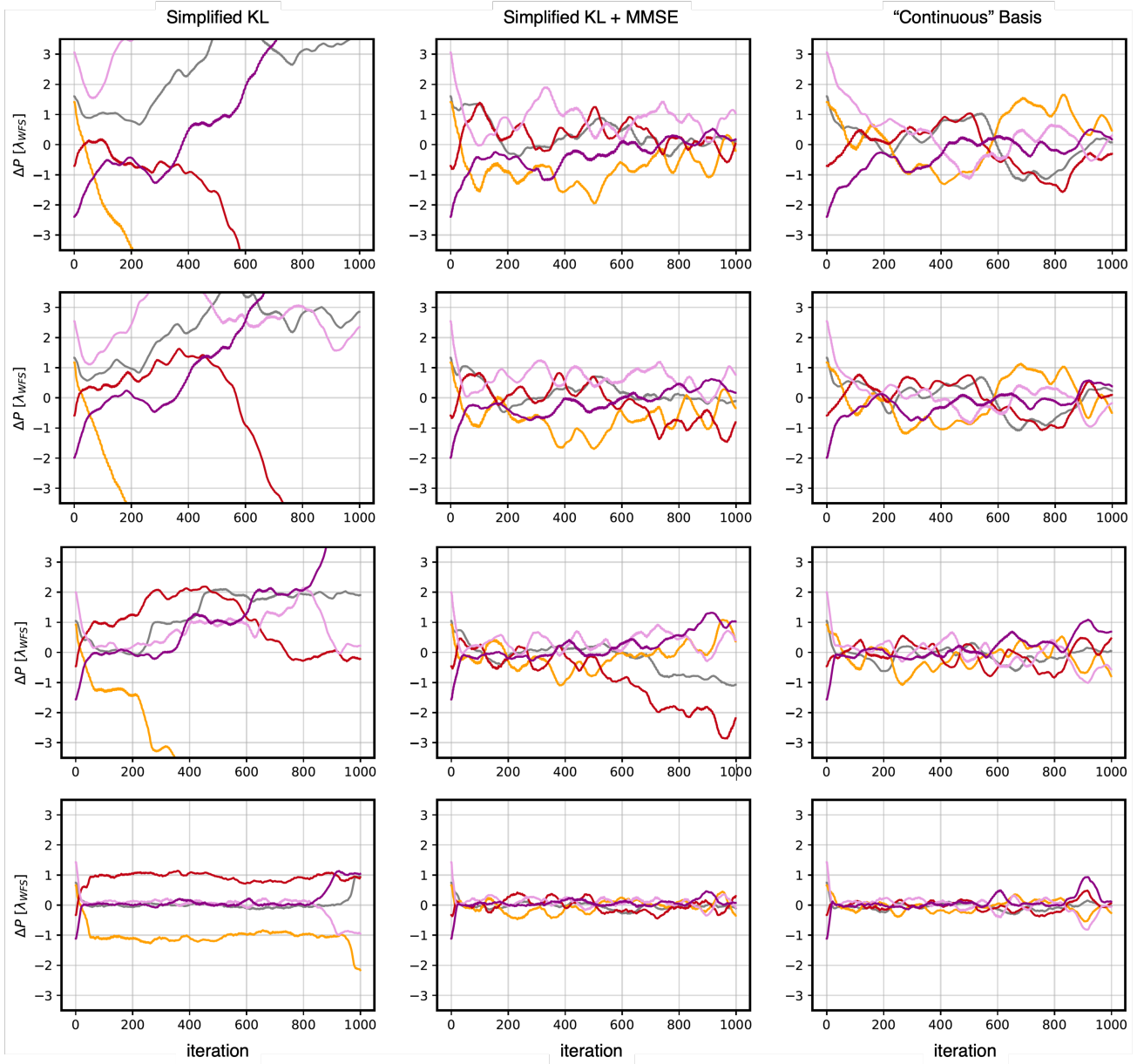


Figure 6. Differential piston fluctuations over 1000 iterations (2 s) for a P-WFS with  $3 \lambda/D$  modulation, based on the residual phase applied on the SLM. *Left* for a regular simplified KL basis, *Middle* when using the "MMSE" reconstruction, *Right* for the "continuous" basis. Each row refers to, from top to bottom, a Fried parameter of  $r_0 = 12, 15, 20, 30$  cm ( $\lambda = 500$  nm).

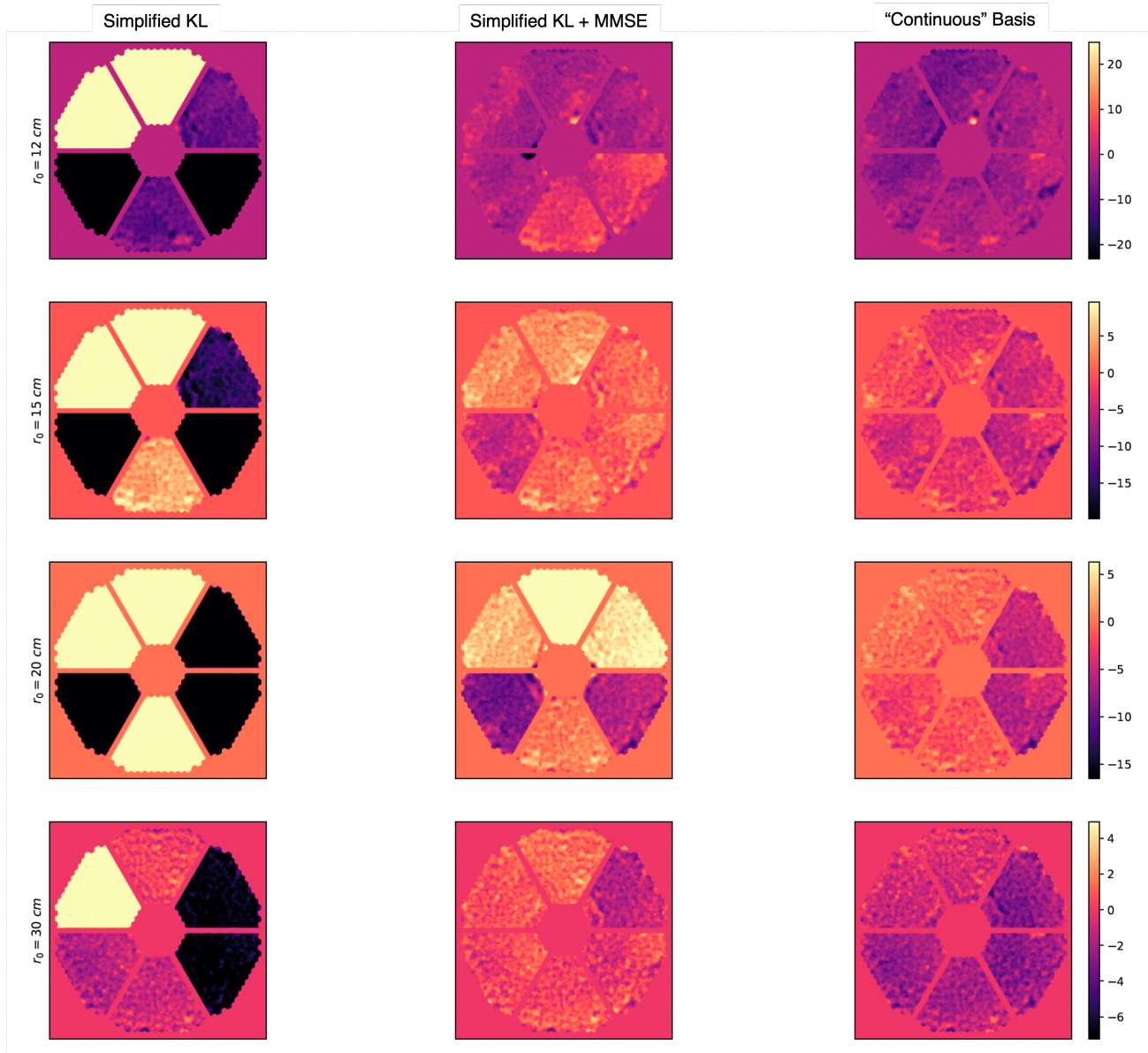


Figure 7. WF residual phase applied on the SLM at iteration 1000 of the AO loop, for a P-WFS with  $3 \lambda/D$  modulation. **Left** for a regular simplified KL basis, **Middle** when using the "MMSE" reconstruction, **Right** for the "continuous" basis. Each row refers to, from top to bottom, a Fried parameter of  $r_0 = 12, 15, 20, 30 \text{ cm}$  ( $\lambda = 500 \text{ nm}$ ). Colorscales are in microns.

## References

- [1] A. Bertrou-Cantou et al. “Confusion in differential piston measurement with the pyramid wavefront sensor”. In: 658, A49 (Feb. 2022), A49. DOI: [10.1051/0004-6361/202141632](https://doi.org/10.1051/0004-6361/202141632).
- [2] Arielle Bertrou-Cantou. “Analyse de front d’onde et commande en optique adaptative pour la pupille fragmentée de l’ELT”. Available at <https://www.theses.fr/2021UNIP7191>. PhD thesis. Université de Paris, Oct. 2021.
- [3] Arielle Bertrou-Cantou et al. “Analysis of the island effect for ELT MICADO MAORY SCAO mode”. In: *Proceedings of the AO4ELT6 conference*. Nov. 2019, E4.
- [4] Bernhard R. Brandl et al. “Status of the mid-IR ELT imager and spectrograph (METIS)”. In: *Ground-based and Airborne Instrumentation for Astronomy VII*. Ed. by Christopher J. Evans, Luc Simard, and Hideki Takami. Vol. 10702. Society of Photo-Optical Instrumentation Engineers (SPIE) Conference Series. July 2018, 107021U, 107021U. DOI: [10.1117/12.2311492](https://doi.org/10.1117/12.2311492).
- [5] Fanny Chemla et al. “SAPHIR: a new concept of reflective pyramidal wavefront-sensor free from chromatic aberrations”. In: *Proceedings of the AO4ELT6 conference*. Nov. 2019, E4.
- [6] Yann Clénet et al. “Joint MICADO-MAORY SCAO mode: specifications, prototyping, simulations and preliminary design”. In: *Adaptive Optics Systems V*. Ed. by Enrico Marchetti, Laird M. Close, and Jean-Pierre Véran. Vol. 9909. Society of Photo-Optical Instrumentation Engineers (SPIE) Conference Series. July 2016, 99090A, 99090A. DOI: [10.1117/12.2231192](https://doi.org/10.1117/12.2231192).
- [7] Yann Clénet et al. “The MICADO first light imager for the ELT: overview of the SCAO module at its final design”. In: *Adaptive Optics Systems VIII*. Ed. by Laura Schreiber, Dirk Schmidt, and Elise Vernet. Vol. 12185. Society of Photo-Optical Instrumentation Engineers (SPIE) Conference Series. Aug. 2022, 121854S, 121854S. DOI: [10.1117/12.2629856](https://doi.org/10.1117/12.2629856).
- [8] V. Deo et al. “Assessing and mitigating alignment defects of the pyramid wavefront sensor: a translation insensitive control method”. In: 619, A56 (Nov. 2018), A56. DOI: [10.1051/0004-6361/201833685](https://doi.org/10.1051/0004-6361/201833685).
- [9] F. Ferreira et al. “Hard real-time core software of the AO RTC COSMIC platform: architecture and performance”. In: *Adaptive Optics Systems VII*. Ed. by Laura Schreiber, Dirk Schmidt, and Elise Vernet. Vol. 11448. Society of Photo-Optical Instrumentation Engineers (SPIE) Conference Series. Dec. 2020, 1144815, p. 1144815. DOI: [10.1117/12.2561244](https://doi.org/10.1117/12.2561244).
- [10] Eric Gendron. personal communication. Feb. 3, 2020.
- [11] C. T. Heritier et al. “A new calibration strategy for adaptive telescopes with pyramid WFS”. In: 481.2 (Dec. 2018), pp. 2829–2840. DOI: [10.1093/mnras/sty2485](https://doi.org/10.1093/mnras/sty2485). arXiv: [1809.04848](https://arxiv.org/abs/1809.04848) [[astro-ph.IM](https://arxiv.org/abs/1809.04848)].
- [12] Victoria Hutterer et al. “Advanced wavefront reconstruction methods for segmented Extremely Large Telescope pupils using pyramid sensors”. In: *Journal of Astronomical Telescopes, Instruments, and Systems* 4, 049005 (Oct. 2018), p. 049005. DOI: [10.1117/1.JATIS.4.4.049005](https://doi.org/10.1117/1.JATIS.4.4.049005).
- [13] B. Neichel et al. “The adaptive optics modes for HARMONI: from Classical to Laser Assisted Tomographic AO”. In: *Adaptive Optics Systems V*. Ed. by Enrico Marchetti, Laird M. Close, and Jean-Pierre Véran. Vol. 9909. Society of Photo-Optical Instrumentation Engineers (SPIE) Conference Series. July 2016, 990909, p. 990909. DOI: [10.1117/12.2231681](https://doi.org/10.1117/12.2231681). arXiv: [1805.11931](https://arxiv.org/abs/1805.11931) [[astro-ph.IM](https://arxiv.org/abs/1805.11931)].
- [14] Noah Schwartz et al. “Analysis and mitigation of pupil discontinuities on adaptive optics performance”. In: *Adaptive Optics Systems VI*. Ed. by Laird M. Close, Laura Schreiber, and Dirk Schmidt. Vol. 10703. Society of Photo-Optical Instrumentation Engineers (SPIE) Conference Series. July 2018, 1070322, p. 1070322. DOI: [10.1117/12.2313129](https://doi.org/10.1117/12.2313129).
- [15] F. Vidal et al. “Tomography reconstruction using the Learn and Apply algorithm”. In: *Adaptive Optics for Extremely Large Telescopes*. Jan. 2010, 07001, p. 07001. DOI: [10.1051/ao4elt/201007001](https://doi.org/10.1051/ao4elt/201007001).
- [16] Fabrice Vidal et al. “Tests and characterisations of the ALPAO 64×64 deformable mirror, the MICADO-MAORY SCAO AIT facility”. In: *Proceedings of the AO4ELT6 conference*. Nov. 2019, E4.